Spin-vibronic coherence drives singlet-triplet conversion

Shahnawaz Rafiq[1], Nicholas P. Weingartz[1,3], Sarah Kromer,[2] Felix N. Castellano[2]*, Lin X. Chen[1,3]*

[1]Department of Chemistry, Northwestern University; Evanston, Illinois, 60208, USA.

[2]Department of Chemistry, North Carolina State University; Raleigh, North Carolina, 27695-8204, USA.

[3]Chemical Sciences and Engineering Division, Argonne National Laboratory, Lemont, Illinois, 60439

*Corresponding author. Email:l-chen@northwestern.edu or lchen@anl.gov; fncastel@ncsu.edu

Design-specific control over transitions between electronic excited states having different spin multiplicities is of utmost importance in molecular and materials chemistry.[1-3] Recent findings suggest that the coincidence of spin-orbit and vibronic effects – collectively termed the spin-vibronic effect – can drastically accelerate this quantum-mechanically forbidden transition at nonadiabatic crossings.[4,5] However, discerning precise experimental manifestations of the spin-vibronic mechanism remains challenging. Here, we present coherence spectroscopy experiments unraveling the coupled interplay between spin, electronic, and vibrational degrees of freedom driving efficient singlet-triplet conversion in four structurally analogous dinuclear Pt(II) metal-metal-to-ligand charge transfer complexes. Photoexcitation activates Pt–Pt bond formation, launching a stretching vibrational wavepacket. The molecular structure-dependent decoherence and recoherence dynamics of this wavepacket resolve the spin-vibronic mechanism. We find that vectorial motion along the Pt–Pt stretching coordinate tunes the singlet and intermediate state energy gap irreversibly towards the conical intersection while subsequently driving the formation of the lowest stable triplet state in a ratcheting fashion. This work suggests the viability of using vibronic coherences as decisive probes[6-9] for disentangling the interplay among spin, electronic, and nuclear dynamics in spin-conversion processes, ultimately inspiring new modular designs for tailoring excited state properties.

Light-induced singlet-triplet (ST) electronic spin conversion remains fundamental in molecular and materials chemistry, being leveraged in solar energy harvesting,[10] molecular photonics,[11] photocatalysis,[12] and photosensitizing applications.[13] The conventional picture of ST intersystem crossing (ISC) promoted explicitly by direct spin-orbit coupling (SOC) between electronically excited states of different spin-multiplicities breaks down when vibronic coupling introduces strong quantum mechanical mixing of electronic spin-states.[14] Consequently, spin, electronic, and vibrational degrees of freedom cannot be treated independently using the Born-Oppenheimer approximation framework, and a more complicated spin-vibronic picture of combined relativistic and non-relativistic quantum mechanical effects emerges. The spin-vibronic effect specifically induces rapid radiationless transitions at particular nuclear configurations.[14]

The spin-vibronic mechanism (SVM) has been predicted to play critical roles in spin crossover,[4] photodynamic therapy,[15] deactivation of DNA bases,[16] and thermally activated delayed fluorescence (TADF).[5] In $[Fe(bpy)_3]^{2+}$ (bpy-bipyridyl), the SVM promoted by Fe–N stretching vibrations was hypothesized to enable spin crossover in <50-fs.[4] In $[Cu(dmp)_2]^+$ (dmp – 2,9-dimethylphenanthroline) an SVM mediated by a pseudo-Jahn-Teller distortion in the angle between the two ligand planes hindered ultrafast ISC.[17] In $[Pt_2(POP)_4]^{4-}$ (POP – pyrophosphite) vibrational coherence transfer from the singlet to triplet state suggested nonadiabatic coupling as the primary mechanism for ISC.[18] In donor-acceptor complexes, the SVM adequately described the rate and efficiency of TADF.[5] Despite the apparent ubiquity of spin-vibronic effects, detecting its manifestation in real-time remains elusive. Precise experimental tracking of its mechanism, trajectories, and dynamics can inspire quantum-regulated synthetic design principles for controlling ST conversion through informed structural and compositional modifications beyond simply modifying direct SOC.

Here, we unravel the SVM that drives efficient ST conversion in a series of structurally-related dinuclear Pt(II) complexes by tracking their vibrational wavepacket dynamics using chirp-controlled broadband pump-probe spectroscopy (BBPP) and two-dimensional electronic spectroscopy (2DES). The wavepacket along the Pt–Pt stretching mode exhibits unique molecular structure-dependent decoherence dynamics that correlate strongly with the timescale of ISC. Interestingly, we uncovered spontaneous generation of vibronic coherence along the same Pt–Pt stretching mode following ISC in the impulsive rate limit, revealing an elusive intermediate triplet state that couples nonadiabatically to the photoexcited singlet state. We deduced how the Pt–Pt stretching coordinate, with sequential expansion and contraction of the Pt–Pt bond distance, vectorially tunes the multi-level spin and electronic dynamics, efficiently populating the lowest-lying triplet state.

The molecules investigated (Fig. 1a, coded as **Pt1**–**Pt4**[19]) are Pt(II) dimeric complexes joined by two 6-substituted-2-hydroxypyridyl bridging ligands having pseudo-two-fold symmetry. At sufficiently short inter-Pt(II) distances, the σ-interactions between the $5d_{z^2}$ orbitals enable metal-metal-to-ligand charge-transfer (MMLCT) transitions.[19,20] Structural differences in the bridges (6-methyl in **Pt1** and **Pt2**; 6-phenyl in **Pt3** and **Pt4**) and the cyclometalating ligands (2-phenylpyridine in **Pt1** and **Pt3**; benzoquinoline in **Pt2** and **Pt4**) modifies electronic state energies, affecting the rate of ISC.[20] Excited state energetics and SOC depend on the distance and relative orientation of interacting cofacial $5d_{z^2}$ orbitals dynamically modulated by the Pt–Pt stretching vibration.[21]

Broadband laser pulses compressed to ~7-fs were used to generate superpositions of vibrational states, resulting in vibrational wavepackets or coherences along the Franck-Condon active modes of the four molecules. These coherences are subsequently probed by another laser pulse(s) delayed with respect to the pump pulse, using BBPP and 2DES apparatus.[22] The probe pulse detects the phase-evolution of vibrational coherences as superimposed oscillatory features on the electronic population dynamics, from which the frequency spectrum of the vibrational modes is extracted by taking the Fourier transform (FT) of the oscillations.[8] The laser spectrum spans 500–670 nm (~20000–14900 cm^{-1}) and resonantly excites the ^{1}MMLCT transition (Fig. 1b). All molecules undergo ISC from the photoexcited ^{1}MMLCT to the ^{3}MMLCT state on sub-picosecond timescales.[19,20] The BBPP spectra of **Pt1**-**Pt4**, dominated by triplet state absorptions, feature oscillations in the time-domain signal, indicative of vibrational coherences modulating the transient signals of the electronic states (Fig. 1c).

The integrated FT spectra from BBPP of **Pt1**-**Pt4** reveal two vibrational coherences that peaked near 110 and 150 cm^{-1} (Fig. 1d), with noticeable variations in their relative intensities, shapes, and widths. **Pt1** displays a 107 cm^{-1} band much narrower than the 147 cm^{-1} band; **Pt2** shows no distinct band in the 150 cm^{-1} region but a broad attenuated feature on the higher frequency side of the 112 cm^{-1} band; **Pt3** and **Pt4** feature a narrow, intense band at 145 and 148 cm^{-1} respectively, and a broad, significantly attenuated feature in the ~110 cm^{-1} region. Variations in the intensities, shapes, and widths in their FT peaks, despite structural similarity and dynamics, likely originate from nontrivial electronic-nuclear dynamics and report on the intertwined spin, electronic, and vibrational dynamics. Unraveling the intricacies between vibrational coherences and ISC requires knowledge of the state origins of these coherences, i.e., from the ground, singlet, or triplet electronic states, as well as their dephasing dynamics.

The origin of these vibrational coherences was revealed using the state-selectivity of positively- and negatively-chirped (PC and NC) pump pulses in BBPP spectroscopy. Conceptually, a PC pump pulse disfavors ground-state wavepacket generation whereas an NC pump pulse favors its formation.[23] Thus, one can identify the state origin of the vibrational coherence by monitoring the FT bands' relative intensity under chirped laser pulse excitation. **Pt1** has two FT bands at 107 and 147 cm^{-1}, the former gaining intensity when excited by an NC pulse and losing intensity upon PC pulse excitation, Fig. 2a, upper panel. Conversely, the 147 cm^{-1} band loses intensity under NC pulse excitation and gains intensity when the PC pulse was used (Fig. 2a, lower panel); **Pt2** exhibits similar trends, Extended Data Fig. 1. These observations confirm that the ~110 and ~150 cm^{-1} bands in **Pt1** and **Pt2** respectively originate on the ground and ^{1}MMLCT states. The excitation-detection beat-maps of these bands in **Pt1** constructed from 2DES (Extended Data Fig. 2) support these assignments as the spectrally resolved intensities of these bands peak at the ground state bleach (GSB) and stimulated emission signals, respectively. The higher frequency vibration observed in the excited state results from shortening the Pt–Pt bond by ~0.25Å during the ^{1}MMLCT transition.[20]

The dephasing dynamics of the coherences in **Pt1** and **Pt2** were modeled by nonlinear least squares fitting of the raw time-domain oscillations using exponentially decaying cosine functions (Fig. 2b). For **Pt1**, fitting the oscillatory traces at ω_{probe} = 18200 cm^{-1} and ω_{probe} = 16200 cm^{-1} revealed dephasing time-constants ($\tau_{\text{dephasing}}$) of 615±60 fs and 460±40 fs, corresponding to the ground and excited state vibrational coherences at 107 and 147 cm^{-1}, respectively. For **Pt2**, the respective dephasing time constants of the ground and excited state coherences were 505±55 fs (ω_{probe} = 18000 cm^{-1}) and 290±40 fs (ω_{probe} = 15500 cm^{-1}). Probe frequencies were selected because they constitute a predominantly singular oscillatory component. The dephasing time-constants estimated from nonlinear least squares fitting are within ±60 fs of the time-constants obtained from the Lorentzian lineshape widths (Fig. 2c) of the FT bands ($\tau_{\text{Pt1,107}}$ = 617 fs, $\tau_{\text{Pt1,147}}$ = 420 fs, $\tau_{\text{Pt2,110}}$ = 440 fs, $\tau_{\text{Pt2,140}}$ = 280 fs). Further, a multipeak fitting procedure using Lorentzian lineshapes was also extended to chirped excitation conditions (Extended Data Fig. 3, Table 1). These results illustrate the Pt–Pt vibrational coherence on the singlet state in **Pt1** ($\tau_{\text{dephasing,singlet}}$=460 fs) and **Pt2** ($\tau_{\text{dephasing,singlet}}$=290 fs) dephase faster than their ground states. The vibrational coherence does not transfer to the triplet states even though the electronic population transfers rapidly from the singlet to the triplet manifold. Instead, the vibrational coherence becomes wholly attenuated in the ^{1}MMLCT state of **Pt1** and **Pt2** at the same rate as the ISC.

The ISC-rate-limited decoherence of the Pt–Pt wavepacket in the ^{1}MMLCT state illustrates how this vibration enables the SVM. The induced decoherence is ascribed to the energy-tuning capability of this vibration bridging the singlet and triplet manifolds that promote ISC and prevent coherence survival through the conical intersection, suggesting the SVM at play. The rapidly changing character of the electronic states due to motion along the energy-tuning Pt–Pt vibration and large anharmonicities near the conical intersection appear responsible.[24-26] Similar behavior has been observed for tuning modes in rhodopsin isomerization,[27,28] and promoter modes in near-ballistic electron transfer reactions.[9,29] Besides a few weak high-frequency ligand-centered modes (1200 – 1600 cm^{-1}) revealed by 2DES, no other Franck-Condon mode activity was observed experimentally (Extended Data Fig. 4).

Identifying the triplet electronic state intersecting with the singlet state remains contentious towards invoking the SVM.[5,14,30-33] A distinct feature of the vibrational coherence dynamics in **Pt3** and **Pt4** is the narrow and intense band at 145 and 148 cm^{-1}, respectively (Fig. 1d). Instead of exhibiting monotonic intensity decay kinetics, the amplitude of their oscillations features an initial growth followed by a longer decay (Fig. 3). 2DES beat-maps of these two bands peak at the ^{3}MMLCT absorption signal (Extended Data Fig. 5). Chi-squared analysis of the FT lineshape fitting indicates these bands conform to Gaussian lineshape contrary to the Lorentzian lineshapes in **Pt1** and **Pt2** (Extended Data Fig. 6), suggesting distinct generation and dissipation mechanisms in the coherences in **Pt3** and **Pt4** concerning those observed in **Pt1** and **Pt2** (see Methods).[34] BBPP beat-maps illustrate the spectrally-resolved amplitude of these bands in **Pt3** and **Pt4** do not shift to lower probe energy with respect to the GSB, as observed in **Pt1** and **Pt2** (Extended Data Fig. 7). Additionally, oscillatory maps of the 145 cm^{-1} frequency band in **Pt3** (148 cm^{-1} in **Pt4**) display a phase flip in their oscillations, evidenced by a node of zero amplitude at ω_{probe} = ~16300 cm^{-1} for **Pt3** (ω_{probe} = ~15000 cm^{-1} in **Pt4**), shifting towards lower probe frequency with time (Extended Data Fig. 8). The position of the node occurs in the same spectral region as the triplet absorption peaks.

Therefore, the persistent 145 and 148 cm^{-1} vibrational coherences in **Pt3** and **Pt4** do not originate from the ^{1}MMLCT state; instead, they originate from the ^{3}MMLCT state, where ISC spontaneously generates them in the impulsive rate limit. Due to the impulsive generation of these coherences on the triplet state through ISC – not by direct laser excitation – the chirp-dependent BBPP measurements of **Pt3** and **Pt4** do not exhibit similar correlations in the FT band intensities concerning **Pt1** and **Pt2** (Extended Data Fig. 9). Previous examples supporting the spontaneous generation of coherences due to an impulsive reaction rate include electron transfer at a dye–semiconductor interface,[35] electron transfer in a system of acceptor dissolved in a donor solvent,[9] and a theoretical prediction where vibrational coherence was generated along a mode that directly drives the curve crossing.[36] The extended dephasing times indicate that the lifetime of the corresponding electronic state is long, and the higher frequency suggests a more significant force constant due to the contracted Pt–Pt equilibrium distance in the ^{3}MMLCT state.

A map of oscillations obtained by inverse Fourier filtering of the sharp peak centered at 148 cm^{-1} in **Pt4**, along with the broad feature, displays more robust oscillations up to ~700 fs, followed by persistent but relatively less intense oscillations (Fig. 3a). The filtered inverse FT trace is overlayed with the raw oscillatory trace for a representative ω_{probe} = 17000 cm^{-1} to illustrate that filtering-induced artifacts are insignificant. Nonlinear least squares fitting of the raw oscillations at ω_{probe} = 18000 cm^{-1} reveal a predominantly single frequency component of ω = 120 cm^{-1} with $\tau_{\text{dephasing}}$= 320±55 fs (Fig. 3b). This ~120 cm^{-1} frequency component ($\tau_{\text{dephasing}}$= 290±70 fs) was also observed in the fitting of the oscillations at ω_{probe} = 17000 cm^{-1} in addition to the 148 cm^{-1} frequency component. Fitting the 148 cm^{-1} oscillatory component required simultaneous exponentially growing and decaying cosine functions (Fig. 3b). At ω_{probe} = 17000 cm^{-1}, for the148 cm^{-1} oscillations, $\tau_{\text{dephasing,growth}}$ = 800±240 fs (negative amplitude) and $\tau_{\text{dephasing,decay}}$ = 1060±280 fs (positive amplitude) were observed. The growth and decay components' time constants (and amplitudes) for the 148 cm^{-1} mode feature a strong probe frequency dependence ranging from 500-1000 fs for the $\tau_{\text{dephasing,growth}}$ component and 1-2 ps for the $\tau_{\text{dephasing,decay}}$ component. The growth of the 148 cm^{-1} in **Pt4** oscillations can be observed when the frequency filtering window selected only the sharp band at 148 cm^{-1} (Fig. 3c). The more robust oscillations in the initial ~700-fs time window appear attenuated. Sliding the window to the broad and weaker lower frequency band revealed short-lived but intense oscillations in the same ~700-fs window (Fig. 3d). This was further supported by the FT of the oscillatory trace windowed from t_2=500-fs to 3-ps at a representative ω_{probe} = 17000 cm^{-1} showing only the 148 cm^{-1} component (Extended Data Fig. 10). Nonlinear least squares fitting of **Pt3** revealed similar vibrational coherence dynamics with respective time-constants of $\tau_{\text{dephasing,growth}}$ = 800±120 fs and $\tau_{\text{dephasing,decay}}$ = 1000±140 fs for the 145 cm^{-1} oscillations (Fig. 3e and Extended Data Fig. 11). Such dynamics suggest that the growth of the 145/148 cm^{-1} oscillations is synchronous with the decay of the short-lived oscillations, confirming that they likely originate from two distinct electronic states. Furthermore, the short- and long-lived oscillations have frequencies of ~120 and 148 cm^{-1}, respectively.

ISC impulsively generates the short-lived oscillations at ~120 cm^{-1} in **Pt3** and **Pt4** on a transitory intermediate state of triplet character. The long-lived ~145 cm^{-1} (**Pt3**) and 148 cm^{-1} (**Pt4**) oscillations growing with time-constants of ~500-1000 fs are a consequence of electronic population transfer and the associated vibrational coherences (within the Born-Oppenheimer approximation) from the intermediate state to the lowest ^{3}MMLCT state (<500-fs). The growth in vibrational coherence amplitude parallels the growth in triplet population dynamics. Another contributor could be wavepacket relaxation from upper vibrational levels to the bottom of the potential well.[36] The existence of a close-lying intermediate of ligand-centered $\pi\pi^*$ triplet character having similar equilibrium Pt–Pt distance as the ground state has been predicted by calculations.[20,21] Thus, the Pt–Pt stretching vibration must have a similar frequency in the intermediate and ground states, consistent with our experimental observations. This supports investigations predicting the crucial role of intermediate electronic states in spin conversion based on energetics, symmetry selection rules, and geometry.[4,5,37]

The complete decoherence of the Pt–Pt vibrational wavepacket (~150 cm^{-1}) on the ^{1}MMLCT state – without transferring to the triplet manifold – is a hallmark of spin-vibronic crossing of the electronic states energetically tuned by the Pt–Pt vibration. The ISC process initiates from photoexcitation, preparing the ^{1}MMLCT state with a contracted Pt–Pt distance, interceded by an intermediate state with an expanded Pt–Pt distance. This variation in Pt–Pt geometry bridges the singlet and intermediate energy gap at the conical intersection, and the presence of a SOC leads to spin-vibronic coupling of the states (Fig. 4). Spin-vibronic coupling near the conical intersection lowers the symmetry and induces ultrafast ISC. Due to the impulsive rate of ISC in **Pt3** and **Pt4**, the instantaneous change in the displacement of the Pt–Pt coordinate results in the impulsive generation of vibrational coherence (recoherence) on the intermediate state, which oscillates at

~120 cm^{-1} (Fig. 4). Subsequently, the intermediate state coherence in **Pt3** and **Pt4** transfers to the lowest triplet state due to population transfer in <~500-fs, resulting in a changeover in frequency from ~120 to ~150 cm^{-1} due to the contraction of the equilibrium Pt–Pt distance (Fig. 4). Contrarily, no new coherence was generated in the intermediate states of **Pt1** and **Pt2** because of the slower rate of ISC– not in the impulsive limit – that eventually leads to the absence of any coherence on their lowest ^{3}MMLCT states. These vectorial motions along the Pt–Pt stretching coordinate generate an irreversible population funneling effect driven by an SVM through structural reorganization and relaxation steps that eventually enable efficient ST conversion.

The rates of ISC, and hence the impulsive or non-impulsive ISC, are determined by the position along the Pt–Pt stretching trajectory where the singlet and intermediate states cross in **Pt1**-**Pt4**. Calculations predict that the crossing point is closer to the Franck-Condon geometry in **Pt3** and **Pt4** than in **Pt1** and **Pt2**.[20] Therefore, less energy-tuning is required by the Pt–Pt stretching coordinate to bridge the ^{1}MMLCT-intermediate gap in **Pt3** and **Pt4** than for **Pt1** and **Pt2** (Fig. 4). For this SVM, in addition to tuning the Pt–Pt motion, a coupling mode that is typically a high-frequency vibration is also required.[37] 2DES of each molecule revealed two high-frequency modes of relatively minor Franck-Condon activity with frequencies of ~1243 and ~1305 cm^{-1} (Extended Data Fig. 4), possibly resulting from in-plane breathing vibrations of the coordinated ligands that could potentially act as coupling modes.

The complex interplay of vibrational coherence dynamics (decoherence and recoherence) along the Pt–Pt stretching vibration and ISC trajectory provides unequivocal evidence for the SVM while informing design principles on how molecular structures exploit nonrelativistic quantum mechanics to favor fast and efficient ST population funneling. Applying Pt(II) dimers featuring MMLCT excited states introduced a unique low-frequency vibronic coordinate along the dynamic vibrational motion of the Pt–Pt internuclear axis. Moreover, the steric constraints introduced by the bulkier bridging ligands in **Pt3** and **Pt4** promoted ISC in the impulsive rate limit, ensuring that the conical intersection along the Pt–Pt coordinate lies close to the Franck-Condon geometry, favoring efficient ST spin conversion. These results demonstrate that the interplay of spin, electronic, and nuclear dynamics can defy conventional rules of spin conversion by introducing quantum mechanical funnels. Spin-vibronic effects can have far-reaching implications for a broad range of applications in solar energy conversion, photocatalysis, light-emitting diodes, high-density magnetic data storage, and molecular devices in terms of how quantum mechanics can be used as a tuning element to manipulate or design spin-conversion in functional inorganic, organic, and materials systems even in the absence of heavy atoms.

Online content

Any methods, additional references, Nature Portfolio reporting summaries, source data, extended data, supplementary information, acknowledgments, peer review information; details of author contributions and competing interests; and statement of data and code availability are available at

References

1 An, Z. *et al.* Stabilizing triplet excited states for ultralong organic phosphorescence. *Nat. Mater.* **14**, 685-690 (2015).

2 Wada, Y., Nakagawa, H., Matsumoto, S., Wakisaka, Y. & Kaji, H. Organic light emitters exhibiting very fast reverse intersystem crossing. *Nat. Photonics* **14**, 643-649 (2020).

3 Rao, A. *et al.* The role of spin in the kinetic control of recombination in organic photovoltaics. *Nature* **500**, 435-439 (2013).

4 Auböck, G. & Chergui, M. Sub-50-fs photoinduced spin crossover in [Fe(bpy)3]2+. *Nat. Chem.* **7**, 629-633 (2015).

5 Etherington, M. K., Gibson, J., Higginbotham, H. F., Penfold, T. J. & Monkman, A. P. Revealing the spin–vibronic coupling mechanism of thermally activated delayed fluorescence. *Nat. Commun.* **7**, 13680 (2016).

6 Paulus, B. C., Adelman, S. L., Jamula, Lindsey L. & McCusker, James K. Leveraging excited-state coherence for synthetic control of ultrafast dynamics. *Nature* **582**, 214-218 (2020).

7 Liedy, F. *et al.* Vibrational coherences in manganese single-molecule magnets after ultrafast photoexcitation. *Nat Chem* **12**, 452-458 (2020).

8 Rafiq, S., Bezdek, M. J., Chirik, P. J. & Scholes, G. D. Dinitrogen Coupling to a Terpyridine-Molybdenum Chromophore Is Switched on by Fermi Resonance. *Chem* **5**, 402-416 (2019).

9 Rafiq, S., Fu, B., Kudisch, B. & Scholes, G. D. Interplay of vibrational wavepackets during an ultrafast electron transfer reaction. *Nat. Chem.* **13**, 70-76 (2021).

10 Hedley, G. J., Ruseckas, A. & Samuel, I. D. W. Light Harvesting for Organic Photovoltaics. *Chem. Rev.* **117**, 796-837 (2017).

11 Goushi, K., Yoshida, K., Sato, K. & Adachi, C. Organic light-emitting diodes employing efficient reverse intersystem crossing for triplet-to-singlet state conversion. *Nat. Photonics* **6**, 253-258 (2012).

12 Twilton, J. *et al.* The merger of transition metal and photocatalysis. *Nat. Rev. Chem.* **1** (2017).

13 Zhang, Y. *et al.* Delayed fluorescence from a zirconium(iv) photosensitizer with ligand-to-metal charge-transfer excited states. *Nat. Chem.* **12**, 345-352 (2020).

14 Penfold, T. J., Gindensperger, E., Daniel, C. & Marian, C. M. Spin-Vibronic Mechanism for Intersystem Crossing. *Chem. Rev.* **118**, 6975-7025 (2018).

15 Tatchen, J., Gilka, N. & Marian, C. M. Intersystem crossing driven by vibronic spin–orbit coupling: a case study on psoralen. *Physical Chemistry Chemical Physics* **9**, 5209-5221 (2007).

16 Mai, S. *et al.* The origin of efficient triplet state population in sulfur-substituted nucleobases. *Nat. Commun.* **7**, 13077 (2016).

17 Mara, M. W., Fransted, K. A. & Chen, L. X. Interplays of excited state structures and dynamics in copper(I) diimine complexes: Implications and perspectives. *Coord. Chem. Rev.* **282-283**, 2-18 (2015).

18 Monni, R. *et al.* Vibrational coherence transfer in the ultrafast intersystem crossing of a diplatinum complex in solution. *Proc. Natl. Acad. Sci.* **115**, E6396-E6403 (2018).

19 Chakraborty, A., Yarnell, J. E., Sommer, R. D., Roy, S. & Castellano, F. N. Excited-State Processes of Cyclometalated Platinum(II) Charge-Transfer Dimers Bridged by Hydroxypyridines. *Inorg. Chem.* **57**, 1298-1310 (2018).

20 Kim, P. *et al.* Ultrafast Excited-State Dynamics of Photoluminescent Pt(II) Dimers Probed by a Coherent Vibrational Wavepacket. *J. Phys. Chem. Lett.* **12**, 6794-6803 (2021).

21 Saito, K., Nakao, Y. & Sakaki, S. Theoretical Study of Pyrazolate-Bridged Dinuclear Platinum(II) Complexes: Interesting Potential Energy Curve of the Lowest Energy Triplet Excited State and Phosphorescence Spectra. *Inorg. Chem.* **47**, 4329-4337 (2008).

22 Spencer, A. P. & Chen, L. X. Rapid acquisition of broadband two-dimensional electronic spectra by continuous scanning with conventional delay lines. *Opt. Lett.* **45**, 2942-2945 (2020).

23 Bardeen, C. J., Wang, Q. & Shank, C. V. Selective Excitation of Vibrational Wave-Packet Motion Using Chirped Pulses. *Phys. Rev. Lett.* **75**, 3410-3413 (1995).

24 Kobayashi, Y., Chang, K. F., Zeng, T., Neumark, D. M. & Leone, S. R. Direct mapping of curve-crossing dynamics in IBr by attosecond transient absorption spectroscopy. *Science* **365**, 79-83 (2019).

25 Duan, H.-G. & Thorwart, M. Quantum Mechanical Wave Packet Dynamics at a Conical Intersection with Strong Vibrational Dissipation. *J. Phys. Chem. Lett.* **7**, 382-386 (2016).

26 Peters, W. K., Tiwari, V. & Jonas, D. M. Nodeless vibrational amplitudes and quantum nonadiabatic dynamics in the nested funnel for a pseudo Jahn-Teller molecule or homodimer. *J. Chem. Phys.* **147**, 194306 (2017).

27 Johnson, P. J. M. *et al.* Local vibrational coherences drive the primary photochemistry of vision. *Nat. Chem.* **7**, 980-986 (2015).

28 Kukura, P., McCamant, D. W., Yoon, S., Wandschneider, D. B. & Mathies, R. A. Structural observation of the primary isomerization in vision with femtosecond-stimulated Raman. *Science* **310**, 1006-1009 (2005).

29 Rafiq, S. & Scholes, G. D. From Fundamental Theories to Quantum Coherences in Electron Transfer. *J. Am. Chem. Soc.* **141**, 708-722 (2019).

30 Monni, R. *et al.* Vibrational coherence transfer in the ultrafast intersystem crossing of a diplatinum complex in solution. *Proc. Natl. Acad. Sci.* (2018).

31 Bressler, C. *et al.* Femtosecond XANES Study of the Light-Induced Spin Crossover Dynamics in an Iron(II) Complex. *Science* **323**, 489-492 (2009).

32 Zhang, W. K. *et al.* Tracking excited-state charge and spin dynamics in iron coordination complexes. *Nature* **509**, 345-+ (2014).

33 Lemke, H. T. *et al.* Coherent structural trapping through wave packet dispersion during photoinduced spin state switching. *Nat. Commun.* **8** (2017).

34 Tagliaferro, A., Rovere, M., Padovano, E., Bartoli, M. & Giorcelli, M. Introducing the Novel Mixed Gaussian-Lorentzian Lineshape in the Analysis of the Raman Signal of Biochar. *Nanomaterials (Basel)* **10** (2020).

35 Huber, R., Dworak, L., Moser, J. E., Gratzel, M. & Wachtveitl, J. Beyond Vibrationally Mediated Electron Transfer: Coherent Phenomena Induced by Ultrafast Charge Separation. *J. Phys. Chem. C* **120**, 8534-8539 (2016).

36 Jean, J. M. Vibrational coherence effects on electronic curve crossing. *J. Chem. Phys.* **104**, 5638-5646 (1996).

37 van der Veen, R. M., Cannizzo, A., van Mourik, F., Vlček, A. & Chergui, M. Vibrational Relaxation and Intersystem Crossing of Binuclear Metal Complexes in Solution. *J. Am. Chem. Soc.* **133**, 305-315 (2011).

Figure Captions

Fig. 1| System description and outline of experiments. a, Molecular structures of **Pt1**-**Pt4**. **b,** The visible broadband spectrum (shaded in green) of the laser pulse with ~7-fs pulse duration overlayed on the absorption spectra of the four Pt(II) complexes measured in tetrahydrofuran solvent. **c,** A representative broadband pump-probe map of **Pt4** showing wavepacket oscillations modulating electronic transient absorption signal in the time-domain. **d,** The Fourier transform spectra of **Pt1**-**Pt4** obtained by Fourier transforming the time-domain wavepacket oscillations, integrated over all probe frequencies and normalized at the peak intensities.

Fig. 2| Chirp-dependence, dephasing dynamics, and lineshape analyses of vibrational coherences. a, Integrated Fourier transforms of **Pt1** using transform limited (**TL**), positive chirp of 60 fs^2/rad GVD (**PC1**), positive chirp of 120 fs^2/mm GVD (**PC2**), negative chirp of 60 fs^2/rad GVD (**NC1**), negative chirp of 120 fs^2/mm GVD (**NC2**) laser pulse. Upper and lower panels show FT spectra normalized to the 147 and 107 cm^{-1} peaks respectively. **b,** The exponentially decaying cosine functions were used to fit the raw oscillatory time-domain signal at two probe frequencies for **Pt1** (ω_{probe}=18200 and 16200 cm^{-1}) and **Pt2** (ω_{probe}=18000 and 15500 cm^{-1}). These probe frequencies were chosen because they predominantly had only one oscillatory component. The rapidly oscillating component is due to the THF solvent Raman mode of frequency ~913 cm^{-1}. **c,** Lorentzian fitting of the FT bands corresponding to the raw oscillatory traces at the above probe frequencies in **Pt1** and **Pt2**. The values provided in cm^{-1} units are full-width-half-maximum (FWHM) of the fits. The dephasing time-constants obtained from nonlinear least square fitting in **(b)** are within ±60-fs of the dephasing time-constants obtained from the widths of the Lorentzian fits.

Fig. 3| Spectral Fourier filtering and nonlinear least square fitting reveals a hidden intermediate state. a, Map of oscillatory signals representing windowed FT bands in **Pt4**. A representative inverse-FT is overlayed on the raw oscillatory trace to showcase complete agreement between the two, and that Fourier filtering induced artefacts are negligible. **b,** Nonlinear least square fitting of the raw oscillatory trace of **Pt4** using exponentially decaying cosine functions at ω_{probe}=18000 and 17000 cm^{-1} probe frequencies. The high-frequency oscillating component is due to the 313 cm^{-1} THF solvent Raman mode. **c,** Map of oscillatory signal extracted for the 148 cm^{-1} mode in **Pt4**. The white dashed line is an eye guide tracking the peak amplitude of the oscillations along time as a function of probe frequency. **d,** Map of oscillatory signal corresponding to the broad feature to the low-frequency side of the 148 cm^{-1} peak in **Pt4**. **e,** Nonlinear least square fitting of a representative oscillatory trace at ω_{probe}=17000 cm^{-1} in **Pt3** showing similar dynamics as that of **Pt4**.

Fig. 4| Vibrational coherence dynamics during ISC. The Pt–Pt vibrational wavepacket dynamics during SVM in **Pt1**/**Pt2** (upper panel) and **Pt3**/**P4** (lower panel) is illustrated here. Photoexcitation prepares the Pt–Pt wavepacket on the singlet ^{1}MMLCT state with a contracted Pt–Pt equilibrium position. The singlet wavepacket (~150 cm^{-1}) decoheres completely as the excited state evolves from the Franck-Condon region to the conical intersection. In **Pt3**/**Pt4**, a new vibrational coherence (~120 cm^{-1}) is generated on the intermediate state due to the impulsive rate of the ISC reaction. This transition involves expansion of the Pt–Pt equilibrium bond distance. The intermediate state internally converts to the lowest triplet state leading to initial growth of the wavepacket, which oscillates with ~150 cm^{-1} frequency due to re-contraction of the Pt–Pt equilibrium bond distance.

Methods

Materials

All Pt(II) dimers studied in this work were synthesized and structurally characterized as described in a previous study.[19]

Steady-state spectroscopy measurements

The steady-state absorption spectra of all the complexes dissolved in tetrahydrofuran (THF) solvent were obtained in Shimadzu UV–3600 UV–vis NIR spectrophotometer. The measurements were performed in a 1 mm pathlength quartz cuvettes at room temperature.

Broadband pump probe and 2DES measurements

The 35-fs pulses from a 10 kHz Ti:Sapphire regeneratively amplified laser system (Solstice Ace, Spectra-Physics) seeds a second-harmonic pumped noncollinear optical parametric amplifier (NOPA) producing broadband pulses spanning 520–670 nm. The NOPA output is compressed to the Fourier transform limit by a 4-f pulse shaper (MIIPSBox640, BioPhotonic Solutions) using the MIIPS algorithm, yielding ~7-fs pulses.[22] The compressed pulses then traverse a partially-common path 4-arm interferometer to generate a square BOXCARS beam geometry of three 40 nJ excitation pulses and one reference pulse with computer-controlled pulse delays. The sample was held at the common focus (~40 μm) of the four beams. The 2DES signal field, generated in the direction of the reference pulse, is spatially filtered from the excitation pulses and then coupled into a spectrograph (Shamrock SR-303i, Andor) equipped with a cooled EMCCD camera (Newton, Andor) for detection of signal–reference spectral interferograms.

Rephasing 2D spectra were measured by rapidly scanning coherence time delay (τ) from 0 fs to 120 fs in 5 fs steps. Sub-optical τ steps are unnecessary in the partially-common path interferometer approach since the signal–reference interferogram is acquired in a "quasi-rotating frame" along τ.[22] 2D spectra are acquired sequentially at a range of waiting time (T) delays to track relaxation dynamics. For each sample, 2D spectra were acquired from 50 fs to 3 ps in 5-fs steps. The signal field is isolated from signal–reference interferograms using the Fourier transform spectral interferometry algorithm. After interpolating and transforming the wavelength axis of the signal field to frequency, the signal field is Fourier transformed along the τ dimension to generate the 2D spectrum as a function of excitation frequency (ω_τ) and detection frequency (ω_t). The phase of the 2D spectrum is corrected by comparison to the spectrally-resolved pump–probe spectrum using the projection–slice theorem method. This separates physically meaningful real (absorptive) and imaginary (refractive) components of the 2D spectrum. 2DES beat-map spectra are generated by first subtracting off the population relaxation dynamics and then Fourier transforming the residual oscillations along the T dimension, yielding beat-maps for individual frequency bands as a function of excitation and detection frequencies.

The broadband pump-probe (BBPP) measurements reported in this study were measured in the same 2DES setup by blocking one pump beam and the reference beam. A chopper set at 100 Hz was placed in the pump beam that allows us to measure the change in intensity of the probe beam in presence and absence of the pump beam.

All the sample solutions of the dinuclear platinum complexes dissolved in THF solvent were continuously flowed through the beam path using 1 mm quartz flow cells (from Starna Cells) to avoid any photodegradation. The samples were flowed using a peristaltic pump (from Masterflex) maintaining a flow rate of ~2 ml per minute. PTFE tubing (from MasterFlex) was used as it has high chemical resistance and inertness to THF solvent.

Chirped pulse excitation

The main requirement for performing coherence spectroscopic experiments is the generation and temporal-compression of the broadband laser pulses. In our experiments, we use NOPA to generate the laser pulse spectrum extending ~520-670 nm. These generated laser pulses are spectrally broad, but they are also stretched in time and require phase adjustment between different Fourier components of the pulse to compress it. Typically, the phase mismatch occurs due to the different speed of the Fourier components within the pulse as the pulse travels through air, nonlinear crystals, and other transmissive optics, etc. For a given spectral bandwidth, the theoretically short pulse is known as the Transform Limited (TL) pulse, given by the time-bandwidth product of the pulse. These TL pulses are obtained by optimizing various pulse compressors like prisms, gratings, a combination of prism and a grating, pulse shapers, chirp mirrors, etc. In our case, we used MIIPS pulse shaper. The TL pulses have all the Fourier components locked in the same relative phase. In the simpler terms, all the colors in the pulse arrive at and interact with the sample at the exact same time.

Broadband laser pulses that are not transform limited are identified as the chirped pulses. In the chirped pulses, the different Fourier components of the pulse have shifted relative phase. This chirp is introduced when the pulse travels through dispersive media, as mentioned above. Besides introducing a constant phase shift to the whole spectrum (which does not affect the structure of the pulse), dispersive media also delays some Fourier components of the pulse in time with respect to the other Fourier components. This later effect collectively introduces second-, third-, fourth- and higher-order dispersions. In the visible spectral region, the dispersive optical materials mostly introduce second-order dispersion (significantly larger than the other higher terms) which is also called Group Velocity Dispersion (GVD). This dispersion sweeps the instantaneous frequency of the Fourier components, with respect to the central frequency, and stretches the input pulse in time, thus increasing the pulse duration. If the GVD term is the highest and other higher-order terms are neglected, the laser pulses are identified as linearly chirped pulses, where the instantaneous frequency shifts linearly with time, and the phase changes quadratically.

The linearly chirped pulses, according to the sign of the GVD, can be positively chirped (PC) pulses or negatively chirped (NC) pulses. In the positively chirped pulses, red components temporally precede blue components of the pulse while as in the negatively chirped pulses, red components temporally succeed blue components of the pulse. In our work, the chirp was introduced by either the insertion (which introduces positive chirp) or removal (which introduces negative chirp) of the 1 mm and 2 mm of the UV grade fused silica broadband window (Thorlabs, WG41010R) in the pump beam. The theoretically calculated GVD for the PC pulses with the 1 mm and 2 mm of fused silica window for our laser pulse spectrum were 60 and 120 fs^2/rad respectively. The pulse duration thereby increased from ~7.0 fs to 27±2 fs for the 1 mm and to 37±3 fs for the 2 mm thickness glass. For the NC pulses, the GVD listed above was introduced with opposite signs. Such experiments have been performed previously to identify the ground and excited state character of the vibrational coherences.[23,38-41]

In our case, the experiment was set up by placing two windows of fused silica of thickness 1 mm each in both the pump and probe beams. The MIIPS pulse shaper was then used to optimize the compression that provided transform limited pulses of ~7-fs pulse duration. To run the experiment with the positively chirped pulses of GVD = ~60 fs^2/rad, an additional 1 mm window was introduced in the pump beam only. For GVD = ~120 fs^2/rad, one more 1 mm window was introduced in the pump beam. For negatively chirped measurement of GVD = ~-60 fs^2/rad, one window out of the initial two windows was removed, leaving behind a total of 1 mm fused silica in the pump beam. For another negative chirp measurement of GVD=~-120 fs^2/rad, the other 1 mm window was also removed from the pump beam, leaving no fused silica windows in the pump beam. Using this procedure of the insertion and removal of silica windows, we were able to measure a total of 5 datasets for each sample. These includes transform limited (TL), positive chirp of GVD=~60 fs^2/rad (PC1), positive chirp of GVD=~120 fs^2/rad (PC2), negative chirp of GVD=~-20 fs^2/rad (NC1), and negative chirp of GVD=~-120 fs^2/rad (NC2). In all these experiments, the probe beam was consistently Transform limited.

The concept behind using the chirped pulse excitation to achieve the selectivity in terms of the ground or excited state vibrational coherences was previously laid down using numerical simulations.[42] In terms of field-matter interactions in pump probe spectroscopy, we know that the pump field introduces two field-matter interactions at the exact same time to create a population state and/or coherent vibrational superposition state, called a wavepacket. This wavepacket can be generated in the ground or excited state. In this wavepacket picture,[43] the first pump field-matter interaction generates a wavepacket on the excited state surface which then starts to evolve down the potential energy surface. A second pump field-matter interaction can generate more amplitude of the wavepacket on the excited state surface or it can project the amplitude of the wavepacket from the first field-matter interaction back to the ground state. In the latter scenario, the two field-matter interactions give rise to an impulsive resonant Raman process that generates a strong ground state wavepacket. This process is amplified when the Fourier components of the pump pulse are ordered in a manner such that the low energy components (red) follow the high energy components (blue) of the pulse. Thus, a negatively chirped pulse (red follows blue) favors the generation of nonstationary ground state wavepacket while a positively chirped pulse (blue follows red) discriminates against it.

Thus, introducing a chirp (positive or negative) in the pump pulse provides a unique and highly selective approach to experimentally bias the wavepacket generation on either the ground or excited states.

Nonlinear least squares fitting of oscillatory kinetic traces

The following exponentially decaying cosine function was used to fit the raw oscillations in the time domain to estimate the frequencies and dephasing time-constants of the oscillating components in the experimental kinetic traces.

$$S(t) = y_0 + \sum_{i=1}^{n} a_i * exp\left(-\frac{t}{\tau_i}\right) * \cos(2\pi\omega_i t + \varphi_i)$$

a_i = amplitude of oscillations of i^{th} frequency component
τ_i = dephasing time-constant of i^{th} frequency component
ω_i = frequency of i^{th} frequency component
φ_i = phase of oscillations of i^{th} frequency component

In addition to the above expression, we also used its modified version to accommodate for the growth and decay of the oscillations corresponding to a particular component. For example, in order to fit an oscillating kinetic trace with two frequency components, one of which has only a decaying dynamics while the other has a growing and decaying dynamics.

$$S(t) = y_0 + a_1 * exp\left(-\frac{t}{\tau_1}\right) * \cos(2\pi\omega_1 t + \varphi_1) + \left[\left(\left(a_2 * exp\left(-\frac{t}{\tau_2}\right)\right) + \left(a_3 * exp\left(-\frac{t}{\tau_3}\right)\right)\right) * \cos(2\pi\omega_2 t + \varphi_2)\right]$$

The pre-exponential factor of the exponentially growing component has a negative value while that of the exponentially decaying component has a positive value.

In addition, the following equation was used to determine the dephasing time-constant from the Lorentzian linewidth of the Fourier transform bands.

$$\tau_{\text{dephasing}}(\text{ps}) = \frac{0.315}{v_{\text{width}}(\text{cm}^{-1})} * 33.3$$

Lorentzian and Gaussian lineshapes

The exact lineshape of a vibrational peak (Raman or Infrared) is typically related to the energy dissipation mechanism of the vibrational mode.[34] When all the oscillators are in the same environment and a single dissipation mechanism is at play, Debye relaxation occurs which is characterized by a single lifetime and thus leads to a Lorentzian lineshape of the vibrational peak. On the other hand, if there is some additional broadening associated with the band, which could originate from, for example, different local environments around the oscillators (heterogeneity) or two or more slightly different frequencies overlapping in the same spectral region, that leads to the Gaussian lineshape of the vibrational band.[44]

In all the dinuclear platinum complexes studied here, most of the Fourier transform peaks conform to the Lorentzian lineshape as is typically expected from vibrational lineshapes. However, the two bands; 145 cm^{-1} in Pt3 and 148 cm^{-1} in Pt4 do not conform to the Lorentzian lineshape instead the Gaussian lineshape was used to fit the two bands. Given that all the four complexes are dissolved in the same solvent and their absorption spectra have a similar shape, we expect an insignificant role of heterogeneity in contributing to the Gaussian shape of the main FT bands in the Pt3 and Pt4. The only other factor that could add broadening to the FT band may be due to the slightly different frequency of the vibrational mode in the ensemble. While we cannot categorically ascribe a reason to this broadening, it is likely that the wavepacket generated on the intermediate state due to the ISC process has multiple frequency components owing to the inherent adiabaticity in the conical intersection region. This is evident to some degree in the structure that is associated with the Fourier transform band of ~120 cm^{-1} on the intermediate state. The 120 cm^{-1} wavepacket transfers on a timescale of <500-fs to the final triplet state with a changeover in frequency to 145 cm^{-1} in Pt3 and 148 cm^{-1} in Pt4 and survives for > 3-ps. The multiple Fourier components wrapped in the wavepacket with slightly different frequencies could cumulatively result in the Gaussian lineshape instead of the Lorentzian lineshape.

Spectral Fourier filtering

Broadband pump probe data measured with temporally compressed broadband laser pulses consists of electronic state population dynamics modulated by the wavepackets in the ground and excited states. These modulations appear in the form of ripples or oscillatory signals along the time domain.[45-47] To study these oscillations explicitly we subtract the slow varying population dynamics from the overall dynamics leaving behind residual oscillations. These oscillations are then Fourier transformed to recover the exact mean frequencies of the vibrational modes along which vibrational superpositions or wavepackets were generated. It is highly likely that more than one wavepackets can be modulating the electronic signal and thus Fourier transform spectra can have more than one bands corresponding to different vibrational modes. At times, we want to look at how the amplitude of a selective vibrational wavepacket varies as a function of time, which becomes a challenge when more than one wavepackets are involved. In these circumstances, we apply a procedure called Fourier filtering.

Fourier filtering involves designing a filter in the frequency or time-domain that selects a particular Fourier transform band. In this case, we mostly deal with filtering in the frequency domain and for this, a super-Gaussian window of varying width was designed to selectively filter out a particular Fourier transform band. Applying this filter reduces the intensity of the FT spectrum to zero everywhere outside the super-Gaussian window. The filtered FT band is then inverse Fourier transformed to convert the filtered frequency domain data back to the time-domain. This process can then be applied to oscillatory traces at all the probe frequencies for generation of a filtered oscillations map. Note that, one must be cautious while applying narrow filters, as that can induces artefacts in the signal.

Apart from filtering out selected FT bands or vibrational frequencies, we can also estimate the dephasing time of a vibrational coherence by fitting the oscillating signal to an exponentially decaying cosine function. The period of the cosine function gives the frequency of the vibrations, and the time-constant of the exponential gives the dephasing time of the oscillations.

Attenuated ground state wavepacket in Pt4

It is noteworthy that the 120 cm^{-1} vibrational wavepacket in **Pt4** does not have its origin in ground state because the former not only has been observed to dephase much faster than in **Pt1** and **Pt2** (Fig. 2), but also does not exhibit similar correlation in the FT intensities for chirp dependent excitation and has a multipeak structure. Additionally, we were able to isolate the ground state coherence in **Pt3** plateauing from the broad attenuated feature centered at ~110 cm^{-1}, indicating that the ISC rate in **Pt3** is slower than in **Pt4**, but still within the impulsive rate limit (Extended Data Fig. 11). The lack of a prominent ground state vibrational coherence at the ~110 cm^{-1} frequency in **Pt4** could result from a high-proportion of population transferred within the total time duration of the pump pulse (20-fs) from the ^{1}MMLCT to the intermediate state. This argument is supported by the variational nonrelativistic calculations on a related complex which predicted a 15 fs - 134 fs time constant for ISC.[48] Therefore, a weak impulsive Raman wavepacket would be projected back onto the ground state close to the equilibrium Pt–Pt coordinate which may be hidden underneath the envelope of the FT spectra.

Data availability

All graphed numerical data (Figures 1-3) is available as source data with this paper.

References

38 Bardeen, C. J., Wang, Q. & Shank, C. V. Femtosecond chirped pulse excitation of vibrational wave packets in LD690 and bacteriorhodopsin. *J. Phys. Chem. A* **102**, 2759-2766 (1998).

39 Malkmus, S. *et al.* Chirp dependence of wave packet motion in oxazine 1. *J. Phys. Chem. A* **109**, 10488-10492 (2005).

40 Yoon, M.-C. *et al.* Ultrafast transient dynamics of Zn(II) porphyrins: Observation of vibrational coherence by controlling chirp of femtosecond pulses. *J. Chem. Phys.* **118**, 164-171 (2002).

41 Lanzani, G., Zavelani-Rossi, M., Cerullo, G., Comoretto, D. & Dellepiane, G. Real-time observation of coherent nuclear motion in polydiacetylene isolated chains. *Phys. Rev. B* **69**, 134302 (2004).

42 Ruhman, S. & Kosloff, R. Application of chirped ultrashort pulses for generating large-amplitude ground-state vibrational coherence: a computer simulation. *J. Opt. Soc. Am. B* **7**, 1748-1752 (1990).

43 Pollard, W. T., Lee, S. Y. & Mathies, R. A. Wave packet theory of dynamic absorption spectra in femtosecond pump–probe experiments. *J. Chem. Phys.* **92**, 4012-4029 (1990).

44 Meier, R. J. On art and science in curve-fitting vibrational spectra. *Vib. Spectrosc* **39**, 266-269 (2005).

45 Rafiq, S. & Scholes, G. D. Slow Intramolecular Vibrational Relaxation Leads to Long-Lived Excited-State Wavepackets. *J. Phys. Chem. A* **120**, 6792-6799 (2016).

46 Yoneda, Y. *et al.* Vibrational Dephasing along the Reaction Coordinate of an Electron Transfer Reaction. *J. Am. Chem. Soc.* **143**, 14511-14522 (2021).

47 Rafiq, S., Dean, J. C. & Scholes, G. D. Observing Vibrational Wavepackets during an Ultrafast Electron Transfer Reaction. *J. Phys. Chem. A* **119**, 11837-11846 (2015).

48 Valentine, A. J. S. *et al.* Resolving the ultrafast intersystem crossing in a bimetallic platinum complex. *J. Chem. Phys.* **151**, 114303 (2019).

Acknowledgements The National Science Foundation supported this collaborative research under CHE-1955806 (S.R., L.X.C.) and CHE-1955795 (S.K., F.N.C.). The U.S. Department of Energy, Office of Science, Office of Basic Energy Sciences, Ultrafast Science Initiative, under Contract No. DE-AC02-06CH11357 (N.P.W., L.X.C.).

Author contributions S.R. conceived and led the project, designed and executed the experiments, analyzed the data, and led preparation and writing of the manuscript. N.W. contributed to executing the experiments, S.K. synthesized molecules, F.N.C. and L.X.C. contributed to conceiving the work and designing the experiments, obtained funding, supervised all research, and contributed to writing the manuscript. All authors contributed to the preparation and writing of the manuscript.

Competing interests The authors declare no competing interests.

Additional information

Supplementary information is available for this paper at https://doi.org/

Correspondence and requests for materials should be addressed to LXC and FNC at l-chen@northwestern.edu and fncastel@ncsu.edu

Peer review information

Reprints and permissions information is available at http://www.nature.com/reprints.

Extended Data Figure Captions

Extended Data Fig. 1| Integrated Fourier transforms of **Pt2** in THF solvent obtained from the BBPP measurements under five different excitation pulse conditions. The excitation pulses used in measuring these datasets were Transform-limited (**TL**) pulses of duration (~7-fs) or positively chirped (**PC1** and **PC2**) and negatively chirped (**NC1** and **NC2**) pulses with group velocity dispersion of 60 and 120 fs^2/rad respectively. These FT bands clearly show a peak at 112 cm^{-1} frequency as well as a broad relatively less intense band in its high frequency region. These FT spectra are intensity normalized to the peak amplitude at 112 cm^{-1} band.

Extended Data Fig. 2| Contour plots of 2DES beat-maps of 107 **(a)** and 147 cm^{-1} **(b)** Fourier transform bands of **Pt1** in tetrahydrofuran solvent. The amplitude of the 107 cm^{-1} FT band in this excitation-detection correlation map (beat-map) is distributed in a manner that the contour mostly peaks at the excitation and detection frequency close to the ground state bleach, indicative of its ground state origin. For 147 cm^{-1} FT band, the amplitude of the beat-map is shifted to lower energy along the detection frequency axis relative to the 107 cm^{-1} band, indicative of its origin from the stimulated emission signal, which in turn assigns this FT band to the ^{1}MMLCT excited state. These 2DES beat-maps are obtained by extracting the oscillatory signal in the time-domain from the electronic population signal using a fitting procedure, followed by Fourier transforming the residual oscillations. The selective Fourier transform bands (107 cm^{-1} and 147 cm^{-1} in this case) are filtered and their amplitude is plotted in the 2DES excitation-detection frequency correlation map.

Extended Data Fig. 3| Multipeak fitting procedure applied to the FT bands of the **Pt1 (a)** and **Pt2 (b)** complexes to retrieve the bandwidth and peak frequency of the overlapping bands. The red traces are raw FT traces, and the blue traces are the fitted traces using two Lorentzian functions. This fitting procedure was extended to all the five excitation conditions namely transform limited pulse, two positively chirped pulse cases, and two negatively chirped pulse cases. The red Lorentzian bands at the bottom of each panel with shaded background are the deconvoluted fits to the overlapping bands. This multipeak fitting procedure successfully resolved the width and peak frequency of the broad, less intense band on the high frequency region of 112 cm^{-1} band in **Pt2**. Apparently, the intensity of this broad feature in **Pt2** is too weak in the case of negatively chirped excitation pulse to be resolved clearly. All the fitting parameters from this multipeak fitting procedure are tabulated in Extended Data Table 1 below.

Extended Data Fig. 4| The Fourier transform spectra of all four **Pt** complexes in THF solvent in the range 1100–1800 cm^{-1} are shown. The FT spectrum of the THF solvent is also shown for comparison. These FT spectra are obtained from the 2DES measurements. Most of the peaks in this spectral region are primarily the solvent Raman peaks. Additionally, we can identify peaks that belong to dinuclear platinum complexes. For **Pt2** and **Pt4**, two peaks at 1243 and 1305 cm^{-1} frequencies can be found; for **Pt1** and **Pt3**, 1262 and 1320 cm^{-1} frequencies are found. Since **Pt2** and **Pt4** share the same ligand and **Pt1** and **Pt3** also share the same ligand, it indicates that these frequencies predominantly originate from ligand sites.

Extended Data Fig. 5| Contour plots of 2DES beat-maps of 145 (**a**) and 148 cm^{-1} (**b**) Fourier transform bands of **Pt3** and **Pt4** complexes respectively. The amplitude of the two FT bands in these excitation-detection correlation maps (beat-maps) are distributed in a manner that the contours peak at the excitation and detection frequency coordinates that match with the triplet absorption signal coordinates, suggesting that these wavepackets originate in the triplet state.

Extended Data Fig. 6| Chi-square test (χ^2) of the Fourier transform lineshape fitting is shown. Chi-square is a statistical test used to examine the difference between categorical values from a random sample to judge the goodness of fit between expected and observed results. In simpler terms, the smaller the chi-square value, the greater the probability that there is an insignificant difference between the observed and the fit results. **(a-b) Pt1** Fourier transform band in the region from 0-300 cm^{-1} corresponding to ω_{probe}=18200 cm^{-1} is fitted with a single Lorentzian and Gaussian lineshapes. The χ^2 value for Lorentzian fit is 0.017, which is ~9 times smaller than the χ^2 value of 0.156 for Gaussian fit, indicating that Lorentzian fit is the best fit **(c-d) Pt4** Fourier transform band from 0-300 cm^{-1} corresponding to ω_{probe}=17000 cm^{-1} is fitted with two Lorentzian and Gaussian lineshapes. The χ^2 value for Lorentzian fit is 0.141 which is ~7 times larger than the χ^2 value of 0.019 for Gaussian fit. When the data is constrained to be fitted only for the peak at 148 cm^{-1} **(e-f)** the χ^2 value for Lorentzian fit is 0.116 which is ~10 times larger than the χ^2 value of 0.011 for Gaussian fit. Thus, confirming that Gaussian fit is the best fit for the **Pt4** data.

Extended Data Fig. 7| Broadband pump probe Fourier transform maps of **Pt1**-**Pt4** in THF solvent. These FT maps are generated by removing electronic population signal from the total BBPP signal and then Fourier transforming the residual oscillations. These resultant FT bands correspond to the frequency of the vibrational modes coupled to the electronic transitions. In the **Pt1** and **Pt2** complexes, the higher frequency Fourier transform band at ~150 cm^{-1} frequency is shifted to the lower probe frequency than the band at ~110 cm^{-1} frequency, indicative of the origin of former band from the stimulated emission signal and the origin of the latter band from the ground state bleach signal. In the **Pt3** and **Pt4** complexes, a prominent band is observed at ~150 cm^{-1} frequency with a broad and less intense feature on its low-frequency region.

Extended Data Fig. 8| Phase change in the oscillations- indicated by the appearance of a node, as a function of probe frequency along the waiting time is shown for **Pt3** and **Pt4**. The clarity of the node is enhanced by performing inverse Fourier filtering procedure of the 145 cm^{-1} In **Pt3** and 148 cm^{-1} in **Pt4** modes using a super-Gaussian window. This window explicitly extracts the wavepacket oscillations corresponding to these frequencies, which are otherwise superimposed by other frequency wavepackets.

The nodes can be seen at ω_{probe} = ~16300 cm^{-1} probe frequency for Pt3 and ω_{probe} = ~15000 cm^{-1} for **Pt4**, and as the waiting time increases the position of node shifts towards lower probe frequency, typical of time-dependent energy lowering of the corresponding electronic state. The position of the node is in the same spectral region where triplet absorption peaks, clearly indicating that this wavepacket modulates the electronic signal of the triplet ^{3}MMLCT state.

Extended Data Fig. 9| Integrated Fourier transform spectra of **Pt3** and **Pt4** complexes obtained by integrating the Fourier transform maps at all the probe frequencies in the BBPP data. The five Fourier transform spectra shown in each plot correspond to five different excitation conditions differing in the chirp of the excitation pulse namely Transform limited pulses (TL), positively chirped pulses of GVD = ~60 fs^2/rad, positively chirped pulses of GVD = ~120 fs^2/rad, negatively chirped pulses of GVD = ~-60 fs^2/rad, and negatively chirped pulses of GVD = ~-120 fs^2/rad. Plots **(a)** and **(b)** show the original and normalized Fourier transform spectra of **Pt3** and **(c)** and **(d)** show the original and normalized spectra for **Pt4** complex. In **(b)** and **(d)**, the spectra are normalized to the intense peak of 145 and 148 cm^{-1} frequencies respectively. The shaded area in each plot represents the broad and less-intense feature in the lower frequency region with respect to the main intense band. The absence of any correlation in the peak intensity as a function of chip of the laser pulse indicates that this intense peak most likely originates from the triplet manifold instead of the singlet manifold.

Extended Data Fig. 10| The Fourier transform of a representative oscillatory trace (ω_{probe}=17000 cm^{-1}) windowed from t_2=500 fs to 3 ps in **Pt4** is shown. The initial 500-fs of the data were cut off intentionally to showcase that the oscillations corresponding to the broad Fourier transform band to the lower frequency of 148 cm^{-1} band dephase at a rapid rate. The Fourier transform band shows only sharp peak at ~148 cm^{-1} frequency.

Extended Data Fig. 11| Fourier filtering procedure applied to the BBPP data of **Pt3** complex. The procedure involves filtering out a Fourier transform band of interest by using a super-Gaussian window. The filtered Fourier transform band is then inverse-Fourier transformed to isolate the time-domain signal of the selective band from all other bands in the Fourier transform spectrum. The filter is initially applied to a single oscillatory trace and then extended to the full pump probe dataset. The extracted time-domain signal of a selected Fourier transform band as a function of probe frequency then shows the spectral and time-domain distribution of the amplitude of a particular mode. In this figure, the filter is first chosen to be broad enough to accommodate the whole FT band **(a)** as shown by the shaded area in the top panel. The filtered FT band is then inverse Fourier transformed and overlayed on the original oscillatory trace to show the matching of the original and filtered trace in the middle panel. The map of the oscillations as a function of probe frequency and time (lower panel) to demonstrate how the amplitude of a particular wavepacket is distributed. We notice that with a broad filter, two components can be observed in the map based on the distribution of the amplitude. When the filter is tightened to select the 145 cm^{-1} mode only **(b)** the oscillation amplitude first grows in time up to ~ 1ps and then decay over >3-ps window. Moving the filter to select the broad and less intense FT band only **(c)** shows that the oscillations dephase within a time-window of ~500-fs. The dephasing time of these oscillations corroborates with the growth time of the 145 cm^{-1} mode oscillations. We also selectively filtered out the FT band at 110 cm^{-1} frequency **(d)** that peaks out of the broad and less intense band. These oscillations survive for ~>1-ps time-window.

	Pt1 (Lorentzian fit)		**Pt2 (Lorentzian fit)**		**Pt3 (Gaussian fit)**		**Pt4 (Gaussian fit)**	
	Frequency (cm^{-1})	FWHM (cm^{-1})	Frequency (cm^{-1})	FWHM (cm^{-1})	Frequency (cm^{-1})	FWHM (cm^{-1})	Frequency (cm^{-1})	FWHM (cm^{-1})
TL	107	16.2±0.3	112	25.9±1.2				
	147	25.8±1.7	143	45±10	145	9.9±0.2	148	10.9±0.1
PC1	107	18.5±0.8	112	22.6±0.5				
	147	26.2±2.2	145	47±8	145	12.5±0.2	148	10.9±0.1
PC2	107	15.8±0.6	109	18.4±0.9				
	147	25.5±1.4	141	41±3.8	145	8.9±0.3	148	11.4±0.1
NC1	107	17.9±0.3	111	22.9±0.5				
	147	24.0±0.7	152	--	145	10.0±0.2	148	11.0±0.1
NC2	107	18.6±0.3	110	26.3±0.5				
	147	25.8±0.8	141	--	145	12.5±0.2	148	10.9±0.1

Extended Data Table 1. The peak frequencies (in cm^{-1}) and bandwidth (Full width half maximum in cm^{-1}) of the Fourier transform bands of all four **Pt** complexes retrieved from the multipeak fitting procedure are tabulated. For the **Pt1** and **Pt2** complexes, the fitting parameters of both the bands at ~110 and ~150 cm^{-1} are tabulated, while as for the **Pt3** and **Pt4** complexes, the fitting parameters of only the intense band at ~150 cm^{-1} are shown. For the **Pt1** and **Pt2** complexes, two Lorentzian functions adequately fit the two FT bands, however, for the **Pt3** and **Pt4** complexes, the Lorentzian functions could not fit the data adequately and Gaussian functions were used instead.

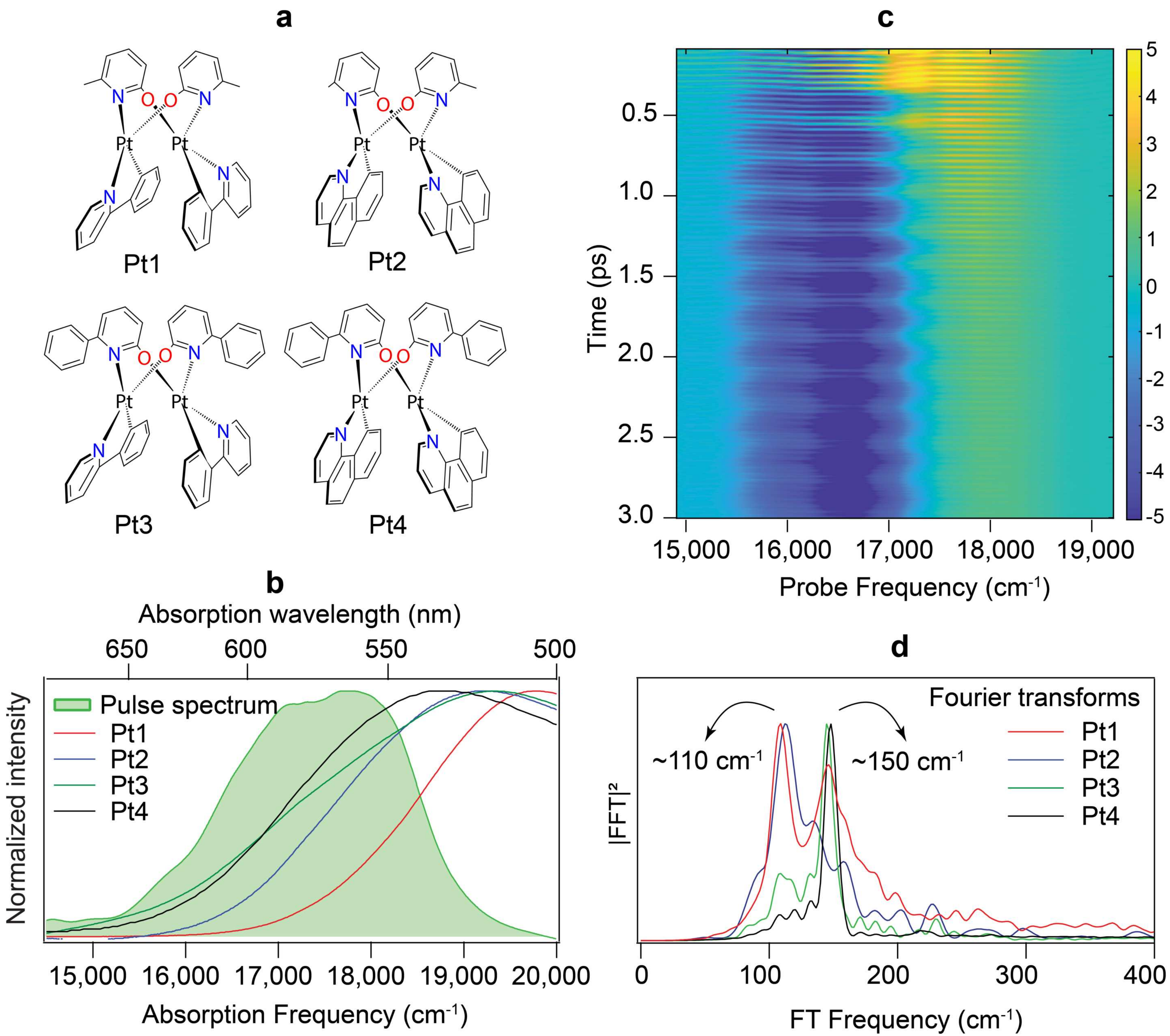

a
Pt1
Pt2
Pt3
Pt4
b
Absorption wavelength (nm)
650
600
550
500
Pulse spectrum
Pt1
Pt2
Pt3
Pt4
Normalized intensity
15,000
16,000
17,000
18,000
19,000
20,000
Absorption Frequency (cm-1)
c
Time (ps)
0.5
1.0
1.5
2.0
2.5
3.0
15,000
16,000
17,000
18,000
19,000
Probe Frequency (cm-1)
5
4
3
2
1
0
-1
-2
-3
-4
-5
d
|FFT|²
Fourier transforms
~110 cm-1
~150 cm-1
Pt1
Pt2
Pt3
Pt4
0
100
200
300
400
FT Frequency (cm-1)

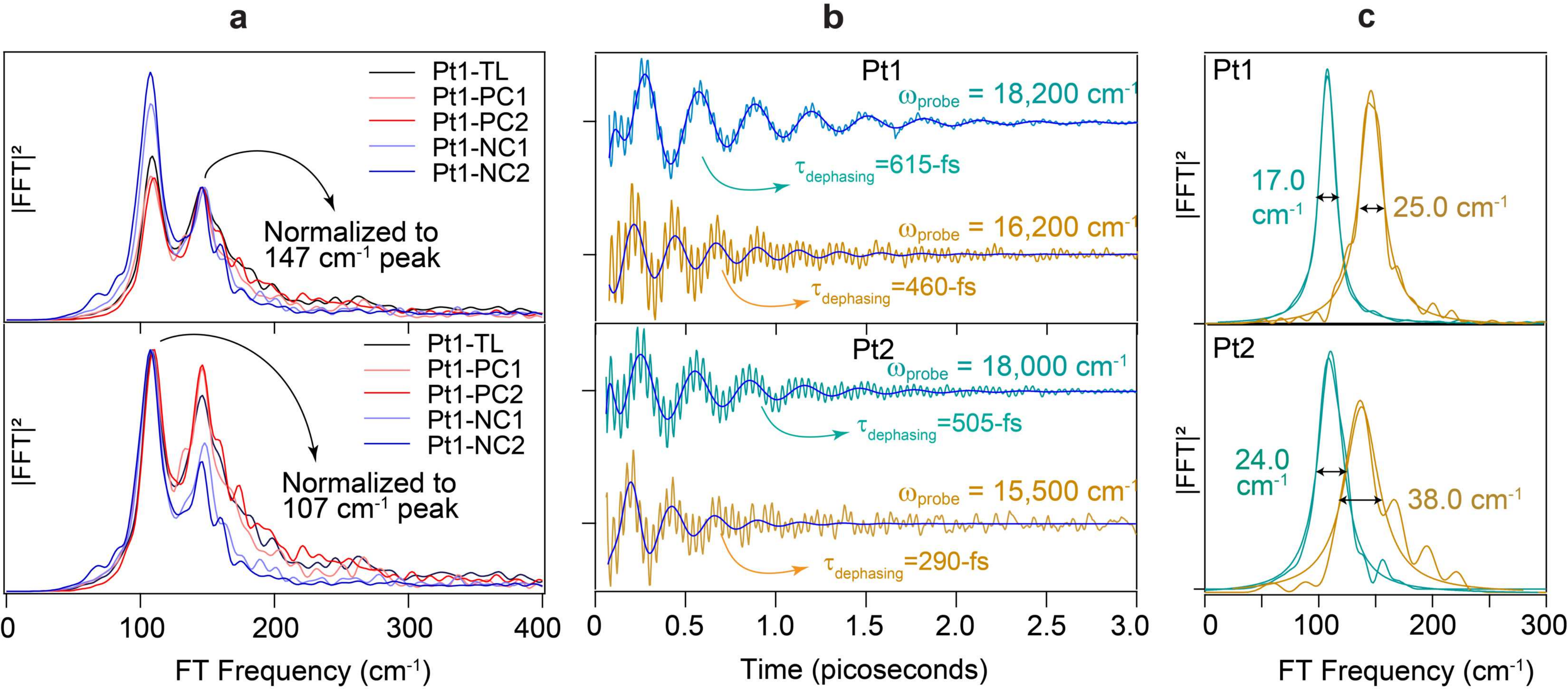
a
b
c
Pt1-TL
Pt1-PC1
Pt1-PC2
Pt1-NC1
Pt1-NC2
|FFT|²
Normalized to 147 cm⁻¹ peak
Normalized to 107 cm⁻¹ peak
FT Frequency (cm⁻¹)
0
100
200
300
400
Pt1
ω_{probe} = 18,200 cm⁻¹
$\tau_{dephasing}$=615-fs
ω_{probe} = 16,200 cm⁻¹
$\tau_{dephasing}$=460-fs
Pt2
ω_{probe} = 18,000 cm⁻¹
$\tau_{dephasing}$=505-fs
ω_{probe} = 15,500 cm⁻¹
$\tau_{dephasing}$=290-fs
Time (picoseconds)
0
0.5
1.0
1.5
2.0
2.5
3.0
Pt1
17.0 cm⁻¹
25.0 cm⁻¹
Pt2
24.0 cm⁻¹
38.0 cm⁻¹
|FFT|²
FT Frequency (cm⁻¹)
0
100
200
300

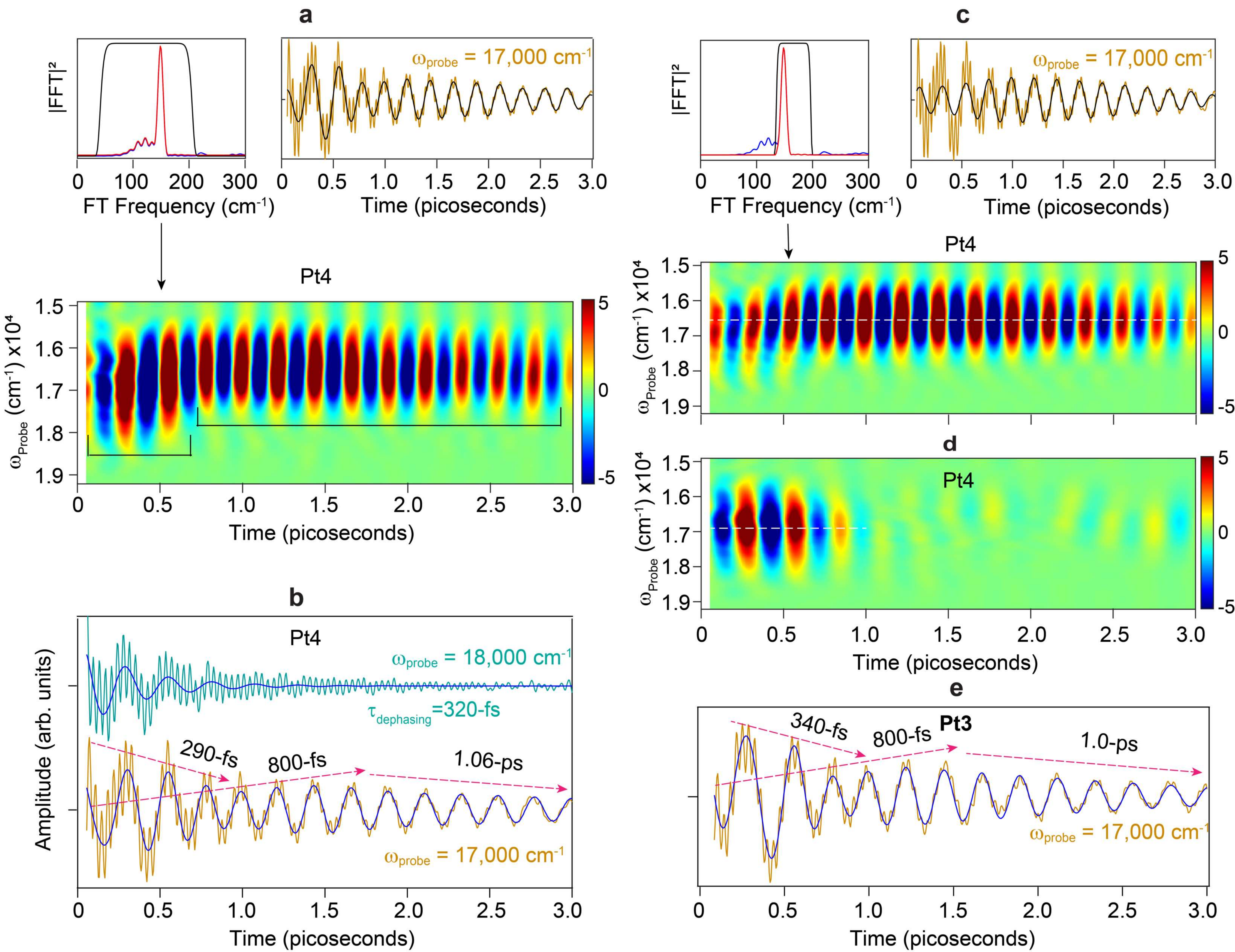
a
|FFT|²
FT Frequency (cm-1)
0 100 200 300
ωprobe = 17,000 cm-1
Time (picoseconds)
0 0.5 1.0 1.5 2.0 2.5 3.0
Pt4
ωProbe (cm-1) x10⁴
1.5 1.6 1.7 1.8 1.9
5 0 -5
b
Pt4
Amplitude (arb. units)
ωprobe = 18,000 cm-1
τdephasing=320-fs
290-fs
800-fs
1.06-ps
ωprobe = 17,000 cm-1
c
|FFT|²
FT Frequency (cm-1)
ωprobe = 17,000 cm-1
Time (picoseconds)
Pt4
d
Pt4
e
340-fs
800-fs
Pt3
1.0-ps
ωprobe = 17,000 cm-1
Time (picoseconds)

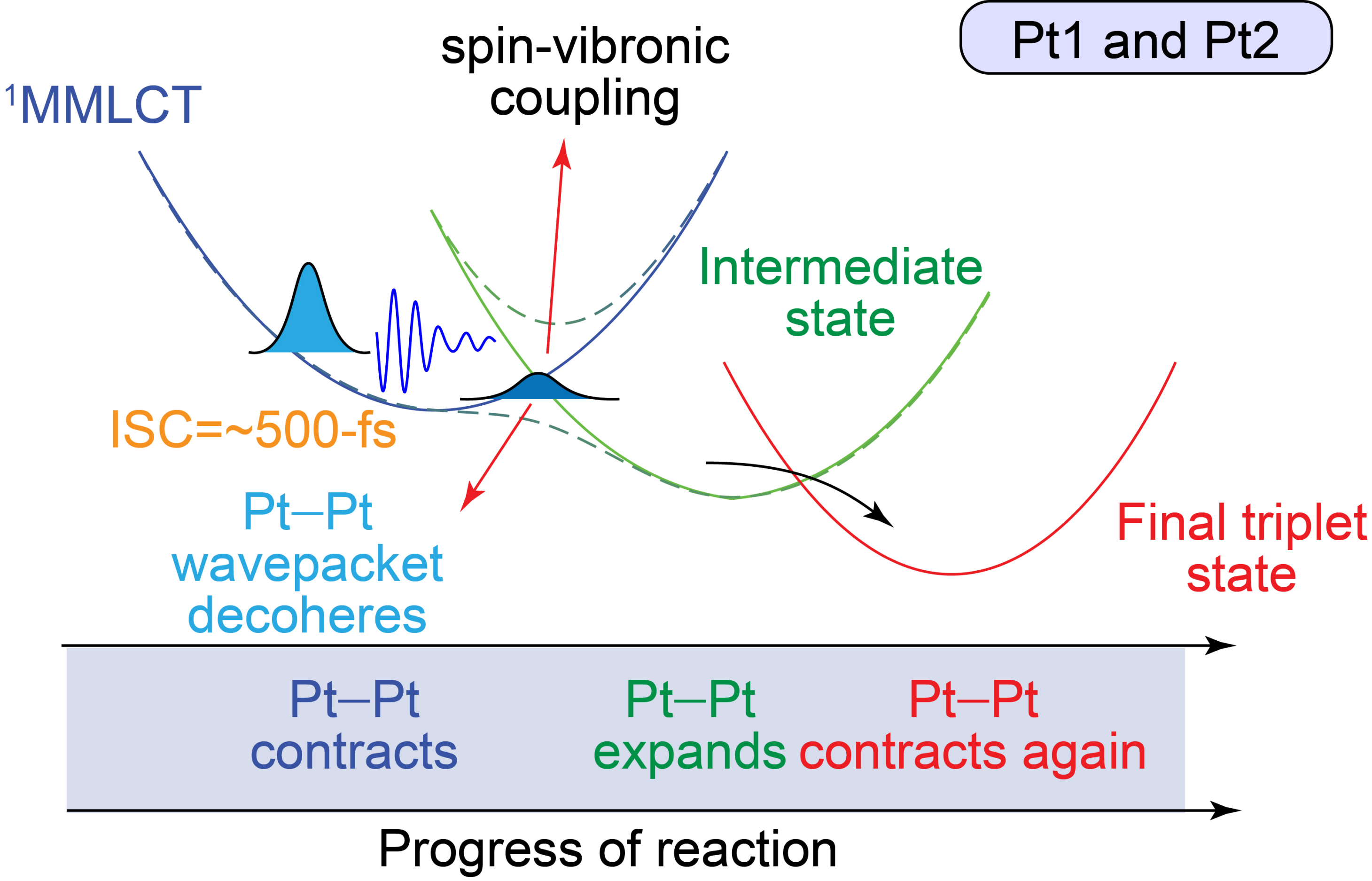
Pt1 and Pt2
spin-vibronic coupling
1MMLCT
Intermediate state
ISC=~500-fs
Pt–Pt wavepacket decoheres
Final triplet state
Pt–Pt contracts
Pt–Pt expands
Pt–Pt contracts again
Progress of reaction

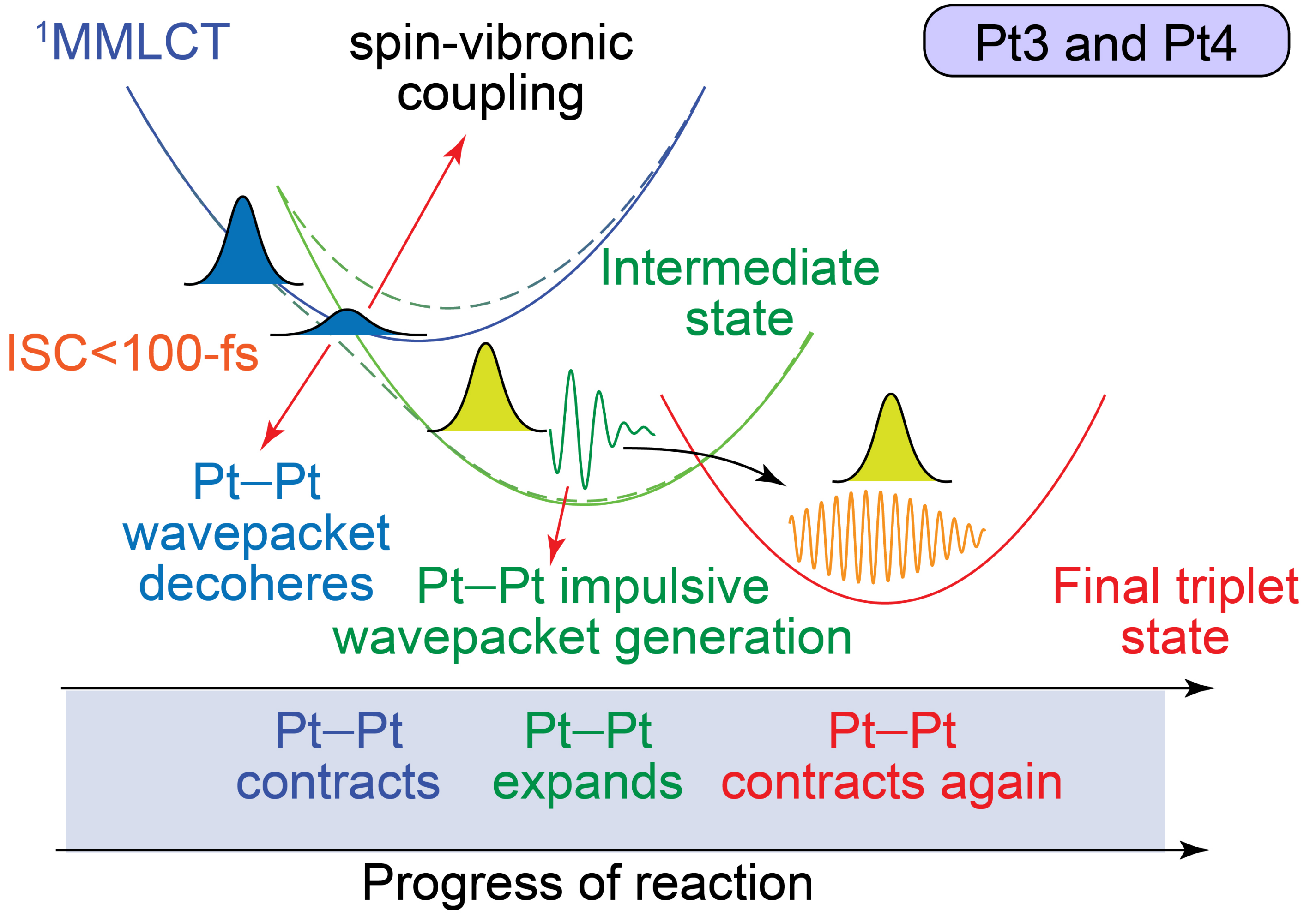
Pt3 and Pt4
1MMLCT
spin-vibronic coupling
Intermediate state
ISC<100-fs
Pt–Pt wavepacket decoheres
Pt–Pt impulsive wavepacket generation
Final triplet state
Pt–Pt contracts
Pt–Pt expands
Pt–Pt contracts again
Progress of reaction